International Journal of Modern Physics B

http://www.worldscinet.com/ijmpb/

IMPACT FACTOR = 1.219

ISSN (print): 0217-9792 | ISSN (online): 1793-6578

Accepted September 6th 2021

Spectral computation of reactive bi-directional hydromagnetic non-Newtonian convection flow from a stretching upper parabolic surface in non-Darcy porous medium

A. Shahid[1], M. M. Bhatti[2*], O. Anwar Bég[3], I. L. Animasaun[4], Khurram Javid[5]

[1]College of Astronautics, Nanjing University of Aeronautics & Astronautics, 210016 Nanjing, ***China***

[2]College of Mathematics and Systems Science, Shandong University of Science & Technology, Qingdao 266590, Shandong People's Republic of ***China***

[3] Professor and Director: Multi-physical Engineering Sciences Group (MPESG), Mechanical Engineering Department, Salford University, Manchester, M54WT, ***UK***

[4]Fluid Dynamics and Survey Research Group, Department of Mathematical Sciences, Federal University of Technology, Akure P.M.B. 704, ***Nigeria***

[5] Department of Mathematics, Northern University, 24110, Wattar-Nowshera, KPK, ***Pakistan***

**Corresponding author: mmbhatti@sdust.edu.cn; mubashirme@yahoo.com*

Abstract: The current article presents a mathematical model for bi-directional convection magnetohydrodynamic (MHD) tangent hyperbolic nanofluid flow from the upper horizontal subsurface of a stretching parabolic surface to a non-Darcian porous medium, as a simulation of nano-coating. Chemical reaction, activation energy and thermosolutal buoyancy effects are included. The Darcy-Brinkman-Forchheimer model is deployed which permits the analysis of inertial (second order) porous drag effects. The Buongiorno nanoscale model is deployed which includes Brownian motion and thermophoresis effects. The dimensionless, transformed, non-linear, coupled ordinary differential equations are solved by implementing the spectral relaxation method (SRM). Validation with previous studies is included. The numerical influence of key parameters on transport characteristics is evaluated and visualized graphically. Velocity is elevated

(and momentum boundary layer thickness is reduced) with increasing wall thickness parameter, permeability parameter, Forchheimer parameter, Weissenberg (rheological) parameter and modified Hartmann (magnetic body force) number. Velocity enhancement is also computed with increment in stretching rate parameter, rheological power-law index, thermal Grashof number, and species (solutal) Grashof number, and momentum boundary layer thickness diminishes. Temperature is suppressed with increasing stretching rate index and Prandtl number whereas it is substantially elevated with increasing Brownian motion and thermophoresis parameters. Velocity and temperature profiles are reduced adjacent to the parabolic surface with larger wall thickness parameter for stretching rate index < 1, whereas the reverse behaviour is observed for stretching rate index>1. Nano-particle concentration magnitude is depleted with larger numeric of Lewis number and the Brownian motion parameter, whereas it is enhanced with greater values of the stretching index and thermophoresis parameter. The nanoparticle concentration magnitude is reduced with an increase in chemical reaction rate parameter whereas it is boosted with activation energy parameter. Skin friction, Nusselt number and Sherwood number are also computed. The study is relevant to electromagnetic nano-materials coating processes with complex chemical reactions.

Keywords: *Bi-directional convection; parabolic coating surface; non-Newtonian nanofluid; porous medium; activation energy; SRM technique.*

1. INTRODUCTION

In 1995, Choi [1] introduced the term “nanofluid” in which nanometer-sized particles e.g. metals (copper, silver, aluminum, zinc, titanium, gold etc.) are suspended in the base fluids, e.g. ethylene glycol, oil, water, and toluene). Nanofluids are, therefore, a subset of molecular fluids operating at the nanoscale. They have stimulated a strong interest in engineering sciences owing to their thermally enhancing properties. *Nanofluid mechanics* provides a robust bridge between bulk materials and molecular or atomic structures. Choi [1] has shown experimentally that nanofluids are stable as long as the size of the nanoparticles is about 100nm. Nanofluids modify the base fluid thermal conductivity [2] and can therefore be used to achieve enhanced cooling, for example in automobile engine radiators, electronic circuits etc. The deployment of nanofluids is expanding also in nuclear reactors, solar renewable energy generation, coolants for lubrication, anti-bacterial (sterilization) systems, aerospace propellants (rocket fuels) and nanomedicine

(cancer therapy) [3-9]. Due to the superior thermal conductivity and convectively heat transfer coefficient of nanofluids [3], these liquids offer significant advantages over conventional base-fluids (e.g., water, air, etc.). The nanoparticles, whether metals or metallic oxides (Cu, Ti, Al, Al_2O_3) etc or non-metals (carbon nanotubes, graphite) in base fluids, both produce enhancement. Mathematical models of nanofluid dynamics have generally adopted one of two approaches. The first is the two-component Buongiorno nanoscale model [10] which includes a formulation for nanoparticle diffusion (concentration) and includes thermophoresis and Brownian dynamics effects; however, it does not permit the analysis of a specific nanomaterial and is confined to a generic nanofluid. The second approach is the Tiwari-Das "single phase model" [11] which although it ignores nanoparticle species diffusion, nevertheless, permits the properties of different nanoparticles and base fluids (e.g. thermal conductivity, viscosity etc) to be quantified via appropriate relationships featuring a solid volume fraction. Via this approach the nanofluid properties can be averaged and thermal modifications in flows can be simulated. Kakaç and Pramuanjaroenkij [12] presented an extensive survey of convective transportation in nanofluids, highlighting major contributions using the Buongiorno and Tiwari-Das approaches.

External boundary layer flows feature frequently in coating dynamics [13]. Numerous surfaces require coating in engineering applications and common processes involve stretching and shrinking plane surfaces, inclined substrates, circular geometries. These often feature heat transfer (thermal coating) [14] and arise in aerospace and marine applications e.g. cylinders for fuselages), spheres for fuel storage tanks, paraboloids for aircraft nose configurations and radomes. Coatings have to be manufactured precisely in these systems also to achieve drag reduction and corrosion/erosion protection [15], 16]. Many researchers have explored the use of nanofluids in coating flows. Bachok *et al*. [17] studied the steady boundary-layer of nanofluid from a translating semi-infinite sheet. Basha *et al*. [18] presented Keller box numerical solutions for entropy generation in tangent hyperbolic nanofluid flow from a circular geometry cylinder with nonlinear Boussinesq approximation, also computing isotherms and streamline distributions. Haddad *et al.* [19] confirmed experimentally the important contributions of Brownian motion and thermophoresis in natural convection flows of nanofluids. Mustafa *et al*. [20] used homotopy and MATLAB bvp4c quadrature to simulate numerically the Hiemenz stagnation flow of a nanofluid from an exponentially stretching sheet, noting that both temperature and the thermal boundary layer thickness are enhanced with greater Brownian motion and thermophoresis effects. They also

observed that increasing thermophoresis effect elevates the nanoparticles volume fraction (concentration). Khan *et al.* [21] presented finite difference computational solutions for the three-dimensional nanofluid flow from an exponentially stretched surface using Buongiorno's model. Ray *et al.* [22] derived homotopy solutions for a variety of external boundary layer thermal coating flows with nanofluids considering flat surfaces, wedges and cones using the Boungiorno two-component model.

In modern materials engineering, engineers are increasingly adopting *functional* designs which permit the manipulation of, for example coating liquids, with external magnetic or electrical fields. These coatings are therefore "smart". The accurate simulation of such flows (e.g. enrobing deposition, spin coating, flame spray finishing etc) [23] involves, in the case of magnetic functional materials [24], the science magnetohydrodynamics (MHD). MHD allows the interaction of magnetic field and fluid flows to be analyzed and also features crystal growth, MHD power generators, MHD sensors, etc. Magnetohydrodynamic Newtonian coating flows have been addressed by Weidner [25] and Conroy and Matar [26]. Nano-coatings utilizing magnetic nanoparticles have been extensively studied experimentally by Triwikantoro *et al.* [27] and Liu *et al.* [28] and have been shown to achieve superior particles distribution, improved morphology and excellent durability for many applications including energy systems [29]. Mathematical models of magnetic nanofluid boundary layer coating flows have also been reported in recent years. Ibrahim and Shankar [30] investigated the magnetic nanofluid flow and heat transfer with velocity, thermal and solutal slip boundary conditions from a permeable stretching sheet. Ibrahim *et al*. [31] explored the MHD nanofluid stagnation point flow from a stretching sheet. MHD boundary layer nanofluid flow with heat transfer towards a nonlinear stretching was analyzed by Mabood *et al.* [32]. All these studies confirmed the strong influence of external magnetic field on nanofluid transport phenomena. However, these investigations ignored *non-Newtonian* behaviour. The presence of nanoparticles in base fluids can dramatically alter the rheology of the resulting colloidal suspension i.e. nanofluid, as confirmed in many studies including Gonçalves [34]. Rheology of nanofluids produces several advantages including water-solubility, electro-optical features, surface plasmon resonance effect-boosted thermal sensitivity, self-improving conductivity and viscosity, all of which contribute to more resilient and intelligent coating designs. A variety of non-Newtonian models have also been deployed to simulate rheological characteristics of nanofluids including Reiner-Rivlin third order viscoelastic models [35], Eyring-

Powell model [36], Casson viscoplastic models [37], power-law (pseudoplastic/dilatant) models and couple stress (polar) models [39]. Another useful model which can accurately predict shear thinning phenomena is the tangent hyperbolic model [40], which has also been implemented in many hydromagnetic coating nanofluid dynamics investigations [41- 44].

A porous medium comprises of solid material fibers interspersed with pores. The enhanced internal surface area has numerous advantages in insulation systems, thermal power technologies and during coating fabrication processes. The increased dissipation area of porous media, for example, achieves improved heat convection compared with conventional substrate coating. Moreover, the tortuosity of porous media also makes them ideal for filtration and damping of flows, providing an excellent control mechanism for coating finishing operations. Low-speed porous media transport (viscous-dominated) is conventionally simulated with the Darcy model [45]. For example, Shamshuddin *et al.* [46] investigated the thermo-capillary coating flow of magnetic nanofluids on a disk in a saturated Darcian porous medium. This and other studies have shown that nanofluids permeating porous media achieve enhanced thermal features, such as convective heat transfer coefficients and higher thermal conductivity as compared with the base material. Hence, nanofluid transport in porous media is attractive from the viewpoint of enhancing the heat transfer characteristics. In certain coating flows, higher velocities arise and inertial (quadratic) porous media drag effects become important. These require non-Darcian models of which the *Darcy–Brinkman–Forchheimer* model [48] is very popular. This model allows the inclusion of viscous diffusion and inertial drag in addition to the conventional Darcy impedance effect. Bhatti *et al.* [47] used the Darcy–Brinkman–Forchheimer model to compute the electro-magnetohydrodynamic flow of a Carreau non-Newtonian liquid in a micro-channel. Elgazery [48] studied MHD rheological nanofluid flow in non-Darcy porous media. Jawad *et al.* [49] analyzed the slip hydromagnetic flow of a magnetic nanofluid with Ohmic dissipation.

The above studies have generally neglected *chemical reaction* effects. Arrhenius activation energy is the least possible energy required to induce chemical reactions and is important in nanomaterials processing operations for optimized synthesis of coating products, chemical reactor design, geothermal engineering, biotechnological manufacturing etc. Several researchers have examined activation energy effects in both viscous flows and more recently in chemo-nanofluid mechanics. Bestman [50] presented on the of the first studies of thermo-solutal natural convection flow with binary reaction and Arrhenius activation in a Darcian porous medium with suction

effects using asymptotic methods. Makinde *et al.* [51] examined the time-dependent natural convective boundary layer flow from a perforated surface with activation energy and nth-order chemical reaction. Hamid *et al.* [52] used a finite difference scheme to compute the impact of activation energy on time-dependent hydromagnetic flow of a Williamson non-Newtonian nanofluid from a stretching cylinder, observing that Nusselt number is reduced with greater reaction rate parameter whereas nanoparticle concentration is elevated with greater activation energy parameter. Irfan *et al.* [53] examined the nonlinear reactive mixed convection in 3D radiative Carreau nanofluid flow with activation energy. Zeeshan *et al.* [54] studied the influence of activation energy on Couette-Poiseuille nanofluid flow with chemical reaction and convective boundary conditions. Khan *et al.* [55] used a shooting numerical method and Buongiorno's nanoscale model to compute the effect of activation energy in hydromagnetic reactive slip flow of a tangent hyperbolic nanofluid from a moving surface with convective boundary conditions. They noted that nanoparticle concentration is enhanced with activation energy parameter and that temperature is elevated with greater Weissenberg (rheological), thermophoresis, Brownian motion and thermal Biot numbers. Bhatti *et al*. [56] used the successive local linearization method (SLLM) to compute the magnetic bioconvection nanofluid flow from a stretching surface in porous media, noting that an increase in chemical reaction constant depletes the nanoparticle concentration whereas the opposite effect is induced with greater activation energy parameter.

An inspection of the literature has shown that thus far, no studies have been reported *on magnetohydrodynamic tangent hyperbolic non-Newtonian nanofluid flowing from a stretching upper parabolic geometry with chemical reaction and activation energy in non-Darcy porous media*. This is the focus of the current study. *The novelty of this work is that it extends previous studies (e.g. Khan et al. [57]) to consider non-Newtonian nanofluid properties with the tangent hyperbolic model and also employs a Darcy-Brinkman-Forchheimer model for porous media effects*. The governing partial differential equations are normalized and rendered into ordinary differential equations by making use of similarity transformations. The resulting nonlinear boundary value problem is solved numerically by employing the spectral relaxation method (SRM) [58, 59]. The present technique shows promising results compared with other similar methods [60-64]. Validation with earlier studies is included. Numerical results for velocity, temperature and nanoparticle concentration are visualized graphically for the influence of key emerging parameters. Extensive interpretation is included. The simulations provide deeper insight into

chemically reactive coating flows of magnetic (smart) nanocoating flows on a complex geometrical substrate.

2. NON-NEWTONIAN HYDROMAGNETIC NANOFLUID REACTIVE COATING FLOW MODEL

Consider the bi-directional steady magnetohydrodynamic (MHD) boundary layer coating flow of a hyperbolic tangent non-Newtonian nanofluid along the upper surface of a stretching parabolic substrate with chemically reacting species. The physical model and Cartesian coordinate system are shown in **Fig. 1**.

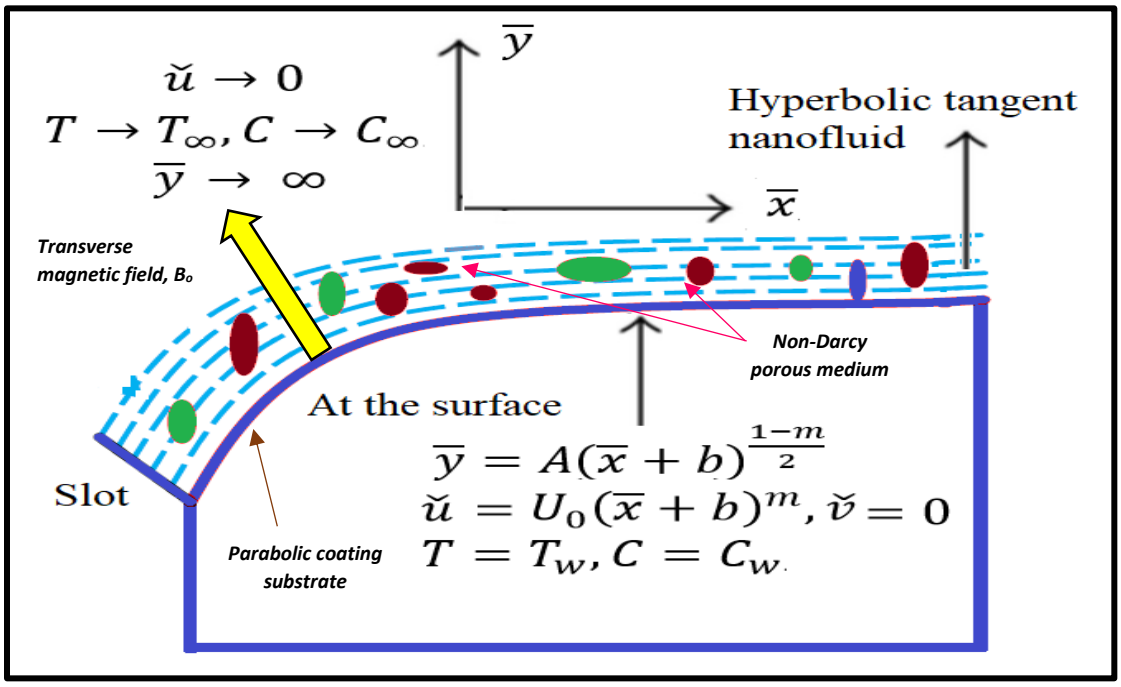

Fig. **1**. Schematic flow diagram.

A magnetic field with strength B_0 is applied in the transverse direction to the surface of the parabola. The parabola wall is stretched with a nonlinear velocity $U_w = U_0(\overline{x} + b)^m$, where m regards as a *stretching index* and U_0 is a reference stretching velocity (linear case). The initial position of the slot subsurface flow is given by $\overline{y} = A(\overline{x} + b)^{\frac{1-m}{2}}$ with $m < 1$. The nanoparticle concentration C_w, and temperature T_w on the subsurface of a parabola are assumed to be constant and greater than the ambient concentration C_∞ and temperature T_∞. Buongiorno's nanoscale model is adopted which features thermophoresis and Brownian motion and a separate

concentration boundary layer equation for nanoparticles. By utilizing the Boussinesq approximation on bi-convection flow, the governing flow equations of *non-Newtonian hyperbolic tangent magnetohydrodynamic reactive nanofluid flow along the parabolic surface* following [57] and [65] may be expressed as:

$$\frac{\partial \breve{u}}{\partial \overline{x}} + \frac{\partial \breve{v}}{\partial \overline{y}} = 0, \tag{1}$$

$$\breve{u}\frac{\partial \breve{u}}{\partial \overline{x}} + \breve{v}\frac{\partial \breve{u}}{\partial \overline{y}} = \nu\left[(n-1)\frac{\partial^2 \breve{u}}{\partial \overline{y}^2} + \sqrt{2}\Gamma\left(\frac{\partial \breve{u}}{\partial \overline{y}}\right)\frac{\partial^2 \breve{u}}{\partial \overline{y}^2}\right] - \frac{\sigma B_0^2}{\rho}\breve{u} + \frac{\partial}{\partial \overline{x}}\left[\tilde{\mathrm{g}}\beta\overline{x}\frac{(m+1)}{2}(T - T_\infty)\right] + \frac{\partial}{\partial \overline{x}}\left[\tilde{\mathrm{g}}\frac{\overline{\beta}(m+1)\overline{x}}{2}(C - C_\infty)\right] - \frac{\mu_f}{\rho k}\breve{u} - \frac{C_F}{\sqrt{k}}\breve{u}^2, \tag{2}$$

$$\left(\breve{u}\frac{\partial T}{\partial \overline{x}} + \breve{v}\frac{\partial T}{\partial \overline{y}}\right) = \alpha\frac{\partial^2 T}{\partial \overline{y}^2} + \tau\left[D_B\frac{\partial T}{\partial \overline{y}}\frac{\partial C}{\partial \overline{y}} + \frac{D_T}{T_\infty}\left(\frac{\partial T}{\partial \overline{y}}\right)^2\right], \tag{3}$$

$$\breve{u}\frac{\partial C}{\partial \overline{x}} + \breve{v}\frac{\partial C}{\partial \overline{y}} = D_B\frac{\partial^2 C}{\partial \overline{y}^2} + \frac{D_T}{T_\infty}\left(\frac{\partial^2 T}{\partial \overline{y}^2}\right) - k_1(C - C_\infty) - k_r^2(C - C_\infty)\left(\frac{T}{T_\infty}\right)^{m_1}\exp\left(\frac{-E_a}{k_0 T}\right). \tag{4}$$

The associated boundary conditions are prescribed as:

$$\left.\begin{aligned}\breve{u}\left(\overline{x}, A(\overline{x}+b)^{\frac{1-m}{2}}\right) = U_w(\overline{x}) = U_0(\overline{x}+b)^m, \breve{v}\left(\overline{x}, A(\overline{x}+b)^{\frac{1-m}{2}}\right) = 0,\\ T = T_w, C = C_w, \qquad \text{at } \overline{y} = A(\overline{x}+b)^{\frac{1-m}{2}},\end{aligned}\right\} \tag{5}$$

$$\breve{u} \to 0, \qquad T \to T_\infty, C \to C_\infty, \qquad \text{as } \overline{y} \to \infty, \tag{6}$$

Here $\alpha = \frac{k}{(\rho c)_f}, \tau = \frac{(\rho c)_p}{(\rho c)_f}$, $\breve{u}$ and $\breve{v}$ are the velocity components in the $\overline{x}$ and $\overline{y}$ directions successively, n the power-law index, $\tilde{\mathrm{g}}$ gravitational acceleration, Γ the time constant, ν is kinematic viscosity, σ, k are the electrical and thermal conductivities of the magnetic nanofluid, T is the temperature, C, C_∞ are the nanoparticle concentration and free stream nanoparticle concentration, respectively, D_B , D_T denote the Brownian-diffusion coefficient and thermophoresis-diffusion coefficient, sequentially, c_p is the specific heat, α is the thermal diffusivity, C_F the Forchheimer coefficient, $\overline{\beta}$ and β are the volumetric solutal and thermal expansion coefficients, k_1 is the reaction rate, k_r the chemical reaction ratio, E_a the activation energy, m_1 denotes the unitless exponent fitted rate constant, and k_0 is the universal gas constant in the Arrhenius exponential reaction term. The new terms introduced in the current model

extending the physics of the current literature are the Forchheimer non-linear drag term $-\frac{C_F}{\sqrt{k}}\breve{u}^2$ and the non-Newtonian term, $+\sqrt{2}\Gamma\left(\frac{\partial\breve{u}}{\partial\overline{y}}\right)\frac{\partial^2\breve{u}}{\partial\overline{y}^2}$ both of which appear in the momentum conservation Eqn. (2). The following similarity transformations are invoked to simplify the primitive equations (1)-(6):

$$\left.\begin{gathered}\psi=\sqrt{\frac{2\nu U_0(x+b)^{m+1}}{(m+1)}}F(\eta),\eta=\sqrt{\frac{(m+1)U_0(x+b)^{m-1}}{2\nu}}\,\overline{y}\\ \breve{u}=U_0(x+b)^m F'(\eta),\quad \breve{v}=-\sqrt{\frac{2\nu U_0(x+b)^{m-1}}{(m+1)}}\left[\frac{(m+1)}{2}F+\frac{(m-1)}{2}\eta F'\right]\\ \theta(\eta)=\frac{T-T_\infty}{T_w-T_\infty},\phi(\eta)=\frac{C-C_\infty}{C_w-C_\infty}\end{gathered}\right\}. \quad (7)$$

Using Eq. (7) in Eqs. (1)-(6), the following *system of the ordinary differential equations for momentum, energy (heat) and nanoparticle concentration* emerge:

$$\begin{aligned}(n-1)F'''+\sqrt{\frac{(m+1)}{2}}nWeF''F'''+FF''-\frac{2m}{m+1}F'^2\\ -\frac{2}{m+1}(\beta_D F'+F_r F'^2+HaF')+Gr_b\theta+R_b\phi=0,\end{aligned} \quad (8)$$

$$\theta''+P_r\left\{F\theta'+\frac{m-1}{m+1}\eta F'\theta'+N_b\,\phi'\theta'+N_t\theta'^2\right\}=0, \quad (9)$$

$$\begin{aligned}\phi''+L_e\left\{F\phi'+\frac{m-1}{m+1}\eta F'\phi'+\frac{N_t}{N_b}\theta''-\frac{2}{m+1}\gamma\phi\right.\\ \left.-\frac{2}{m+1}\sigma_1(1+\delta\theta)^{m_1}e^{\left(\frac{-E}{1+\delta\theta}\right)}\phi\right\}=0.\end{aligned} \quad (10)$$

The transformed boundary conditions at the parabola surface (wall) and in the free stream become:

$$\left.\begin{gathered}F(0)=\frac{(1-m)\alpha_1}{m+1},F'(0)=1,\theta(0)=\phi(0)=1,\\ F'(\infty)=0,\theta(\infty)=\phi(\infty)=0.\end{gathered}\right\} \quad (11)$$

Here:

$$\alpha_1 = A\sqrt{\frac{(m+1)U_0}{2\nu}}, We = \sqrt{\frac{2{U_0}^3(x+b)^{3m-3}}{\nu}}\Gamma, \beta_D = \frac{\mu_f}{U_0(x+b)^{m-1}k},$$

$$Ha = \frac{\sigma {B_0}^2}{\rho U_0(x+b)^{m-1}}, Gr_b = \frac{\bar{g}\beta(T_w - T_\infty)}{(x+b)^{2m-1}{U_0}^2},$$

$$R_b = \frac{\bar{g}(C_w - C_\infty)}{(x+b)^{2m-1}{U_0}^2}, F_r = \frac{C_F(x+b)}{\sqrt{k}}, P_r = \frac{\nu}{\kappa}, N_t = \frac{\tau D_T(T_w - T_\infty)}{\nu T_\infty}, \quad (12)$$

$$N_b = \frac{\tau D_B(C_w - C_\infty)}{\nu}, \gamma = \frac{k_1}{U_0(x+b)^{m-1}}, \sigma_1 = \frac{k_r^2}{U_0(x+b)^{m-1}},$$

$$L_e = \frac{\nu}{D_B}, \delta = \frac{(T_w - T_\infty)}{T_\infty}, E = \frac{E_a}{k_0 T_\infty}.$$

The parameters in Eqn. (12) are respectively wall thickness parameter α_1, Weissenberg (rheological) number We, permeability parametric quantity β_D, Forchheimer parameter F_r, Hartmann magnetic number Ha, the thermal Grashof number, Gr_b, concentration Grashof numbers R_b, Prandtl number P_r, the thermophoresis parameter N_t, the Brownian motion parameter N_b, Lewis number L_e, the chemical reaction constant, σ_1, temperature ratio parameter δ, he activation energy parameter, E and chemical reaction rate parameter, γ, respectively.

Some significant physical parametric quantities in coating dynamics are the skin-friction coefficient "C_F" (dimensionless surface shear stress at the parabola surface), the local-Nusselt number "Nu_x" (dimensionless nanoparticle mass transfer rate at the parabola surface) and the local-Sherwood number "Sh_x" (dimensionless nanoparticle mass transfer rate at the parabola surface). These may be defined for the current flow regime as:

$$C_F Re_x^{\frac{1}{2}} = \sqrt{\frac{(m+1)}{2}}\{(n-1)F''(\eta) + nWeF''(\eta)\}_{\eta=0},$$

$$\frac{Nu_x}{Re_x^{\frac{1}{2}}} = -\sqrt{\frac{(m+1)}{2}}\theta'(0),$$

$$\frac{Sh_x}{Re_x^{1/2}} = -\sqrt{\frac{(m+1)}{2}}\phi'(0), \quad (13)$$

Where $Re_x = \sqrt{\frac{U_0(\overline{x}+b)^{m-1}}{\nu}}$ represents a local Reynolds number.

3. NUMERICAL SOLUTIONS WITH SRM

3.1 The SRM scheme:

Consider a set of non-linear ordinary differential equations in unknown functions i.e, i.e, $f_i(\zeta)$, $i = 1, 2, \dots, n$ where $\zeta \in [a, b]$ is the dependent variable. We define a vector $\boldsymbol{F}_i$ to be a vector of derivatives of the variable f_i for ζ as follow

$$\boldsymbol{F}_i(\zeta) = \left[f_i^{(0)}, f_i^{(1)} \dots f_i^{(p)}, , \dots f_i^{(m)} \right], \tag{14}$$

Where $f_i^{(0)} = f_i$, $f_i^{(p)}$ is the p[th] differential of f_i with respect to ζ, and $f_i^{(m)}$ is the highest differential, respectively. The system can be written as the summation of linear and non-linear terms as follows:

$$\mathcal{L}[\boldsymbol{F}_1, \boldsymbol{F}_2, \dots, \boldsymbol{F}_r] + \tilde{\mathrm{N}}[\boldsymbol{F}_1, \boldsymbol{F}_2, \dots, \boldsymbol{F}_r] = \mathcal{G}_k(\zeta), \; k = 1, 2, \dots, r, \tag{15}$$

Here $\mathcal{G}_k(\zeta)$ is a *known* function of ζ. Eqn. (15) is solved subject to *two-point* boundary conditions which can be symbolized as:

$$\sum_{j=1}^{m} \sum_{p=0}^{m_{j-1}} \alpha_{\upsilon,j}^{(p)} f_j^{(p)}(a) = l_{a,\upsilon}, \quad \upsilon = 1,2, \dots, r_a, \tag{16}$$

$$\sum_{j=1}^{m} \sum_{p=0}^{m_{j-1}} \beta_{\upsilon,j}^{(p)} f_j^{(p)}(b) = l_{b,\sigma}, \quad \sigma = 1,2, \dots, r_b, \tag{17}$$

Here $\alpha_{\upsilon,j}^{(p)}$ and $\beta_{\upsilon,j}^{(p)}$ are the constant coefficients of $f_j^{(p)}$ in the boundary conditions, and ζ_a, ζ_a are the boundary conditions at a and b sequentially.

Now, starting from the initial approximation $\boldsymbol{F}_{1,0}, \boldsymbol{F}_{2,0}, \dots, \boldsymbol{F}_{r,0}$, the iterative method is obtained as

$$\mathcal{L}_1\left[\boldsymbol{F}_{1,r+1}, \boldsymbol{F}_{2,r+1}, \dots, \boldsymbol{F}_{r,r+1}\right] + \tilde{\mathrm{N}}_1\left[\boldsymbol{F}_{1,r}, \boldsymbol{F}_{2,r}, \dots, \boldsymbol{F}_{r,r}\right] = \mathcal{G}_1(\zeta), \tag{18}$$

$$\mathcal{L}_2\left[\boldsymbol{F}_{1,r+1}, \boldsymbol{F}_{2,r+1}, \dots, \boldsymbol{F}_{r,r+1}\right] + \tilde{\mathrm{N}}_2\left[\boldsymbol{F}_{1,r}, \boldsymbol{F}_{2,r}, \dots, \boldsymbol{F}_{r,r}\right] = \mathcal{G}_2(\zeta), \tag{19}$$

$$\vdots \quad \vdots \quad \vdots \quad \vdots \quad \vdots \quad \vdots$$

$$\mathcal{L}_{r-1}\left[\boldsymbol{F}_{1,r+1}, \boldsymbol{F}_{2,r+1}, \dots, \boldsymbol{F}_{r,r+1}\right] + \tilde{\mathrm{N}}_{r-1}\left[\boldsymbol{F}_{1,r}, \boldsymbol{F}_{2,r}, \dots, \boldsymbol{F}_{r,r}\right] = \mathcal{G}_{r-1}(\zeta), \tag{20}$$

$$\mathcal{L}_r\left[\boldsymbol{F}_{1,r+1}, \boldsymbol{F}_{2,r+1}, \dots, \boldsymbol{F}_{r,r+1}\right] + \tilde{\mathrm{N}}_r\left[\boldsymbol{F}_{1,r}, \boldsymbol{F}_{2,r}, \dots, \boldsymbol{F}_{r,r}\right] = \mathcal{G}_r(\zeta), \tag{21}$$

Where $\boldsymbol{F}_{i,r+1}$ and $\boldsymbol{F}_{i,r}$ are the approximations of $\boldsymbol{F}_i$ at the current and precedent iterations, consecutively. Eqns. (18)-(21) establish a set of n linear decoupled equations to be resolved iteratively for $r = 1, 2, \dots$. These iterations commence with an initial approximation $\boldsymbol{F}_{i,0}$ that conforms to the given boundary conditions. The iterations continue until convergence is achieved. Now, the Chebyshev pseudospectral method [33] is implemented at this stage over Eqs. (17) -(20). The differentiation matrix is defined as follow

$$\frac{df_i(\zeta_l)}{d\zeta} = \sum_{K=0}^{N} \mathbf{D}_{lk} f_i(\tau_K) = \mathbf{D}\boldsymbol{F}_i, \; l = 0, \dots, N, \tag{22}$$

Here $N+1$ represents the number of collocation points, $\boldsymbol{D} = 2D/(b-a)$ and $\boldsymbol{F} = [F(\zeta_0), F(\zeta_1), \ldots, F(\zeta_N)\ ]^T$ is the vector function of the collocation points and $\boldsymbol{D}$ for higher-order derivatives are obtained as:

$$f_j^{(p)} = \mathbf{D}^{\boldsymbol{p}} \boldsymbol{F}_i. \tag{23}$$

Thus, for the system of Eqns. (18)-(21), the previously known functions decouple the system of equations and an efficient iteration scheme is established to generate accurate results.

3.2 Solutions by SRM Technique:

The SRM technique is now applied to the present nonlinear ordinary differential Eqns. (8)-(10) and boundary conditions (11). This demands the reduction of the order in the momentum Eqn. (8). Assuming $F' = G$, then Eqns. (8)-(10) assume the form:

$$(n-1)G'' + \sqrt{\tfrac{(m+1)}{2}}nWeG'G'' + FG' - \tfrac{2m}{m+1}G^2 - \tfrac{2}{m+1}(\beta_D G + F_r G^2 + HaG) + Gr_b\theta + R_b\phi = 0, \tag{24}$$

$$\theta'' + P_r\left\{F\theta' + \tfrac{m-1}{m+1}\eta G\theta' + N_b\,\phi'\theta' + N_t\theta'^2\right\} = 0, \tag{25}$$

$$\phi'' + L_e\left\{F\phi' + \tfrac{m-1}{m+1}\eta G\phi' + \tfrac{N_t}{N_b}\theta'' - \tfrac{2}{m+1}\gamma\phi - \tfrac{2}{m+1}\sigma_1(1+\delta\theta)^m e^{\left(\frac{-E}{1+\delta\theta}\right)}\phi\right\} = 0. \tag{26}$$

Next the Gauss-Seidel relaxation technique is deployed to decouple the reduced system into the following form:

$$F'_{s+1} = G_s, \tag{27}$$

$$(n-1)G''_{s+1} + F_s G'_{s+1} - \left(\tfrac{2}{m+1}\right)\{Ha + \beta_D\}G_{s+1} = \left(\tfrac{2m}{m+1}\right)G^2{}_s + \left(\tfrac{2}{m+1}\right)F_r G^2{}_s - \sqrt{\tfrac{(m+1)}{2}}nWeG'{}_s G''{}_s - Gr_b\theta_s - R_b\phi_s, \tag{28}$$

$$\theta_{s+1}{}'' + P_r\left\{F_{s+1}\theta'_{s+1} + \tfrac{m-1}{m+1}\eta G_{s+1}\theta'_{s+1} + N_b\,\phi_s'\theta'_{s+1} + N_t\theta'^2{}_{s+1}\right\} = 0, \tag{29}$$

$$\phi_{s+1}{}'' + L_e\left\{F_{s+1}\phi'_{s+1} + \tfrac{m-1}{m+1}\eta G_{s+1}\phi'_{s+1} + \tfrac{N_t}{N_b}\theta''_{s+1} - \tfrac{2}{m+1}\gamma\phi_{s+1} - \tfrac{2}{m+1}\sigma_1(1+\delta\theta)^{m_1}e^{\left(\frac{-E}{1+\delta\theta}\right)}\phi_{s+1}\right\} = 0. \tag{30}$$

The boundary conditions (11) become:

$$F_{s+1}(0) = \tfrac{(1-m)\alpha_1}{m+1}, G_{s+1}(0) = 1 = \theta_{s+1}(0) = \phi_{s+1}(0), \tag{31}$$

$$G_{s+1}(\infty) = 0 = \theta_{s+1}(\infty) = \phi_{s+1}(\infty). \tag{32}$$

Here the components with indexing "$s+1$" denote the recently approximated data and the components with indexing "s" denote former approximated data. At this stage, the Chebyshev pseudospectral method [58, 59] is implemented in Eqns. (26)-(32), and here the differentiation matrix "$\boldsymbol{D} = \frac{2}{l}D$" is computed for approximate magnitudes of the differentials of undetermined variables in Eqns. (26)-(32), giving:

$$\boldsymbol{D}F_{s+1} = G_s, \tag{33}$$

$$\left\{(n-1)\boldsymbol{D}^2 + diag\left[a_{0,s}\right]\boldsymbol{D} - \frac{2}{m+1}diag\left[a_{1,s}\right]\boldsymbol{I}\right\}G_{s+1} = B_{1,s}, \tag{34}$$

$$\left\{\boldsymbol{D}^2 + +P_r\left\{diag\left[b_{0,s}\right]\boldsymbol{D} + \frac{m-1}{m+1}diag\left[b_{1,s}\right]\boldsymbol{D} + N_t\boldsymbol{D}^2\right\}\right\}\theta_{s+1} = B_{2,s}, \tag{35}$$

$$\left\{\boldsymbol{D}^2 + +L_e\left\{diag\left[c_{0,s}\right]\boldsymbol{D} + \frac{N_t}{N_b}diag[\theta''_{s+1}] - \frac{2}{m+1}\gamma - \frac{2}{m+1}diag\left[c_{1,s}\right]\right\}\right\}\phi_{s+1} = B_{3,s}. \tag{36}$$

The related boundary conditions emerge as:

$$F_{s+1}(\eta_N) = \frac{(1-m)\alpha_1}{m+1}, G_{s+1}(\eta_N) = 1 = \theta_{s+1}(\eta_N) = \phi_{s+1}(\eta_N), \tag{37}$$

$$G_{s+1}(\eta_0) = 0 = \theta_{s+1}(\eta_0) = \phi_{s+1}(\eta_0). \tag{38}$$

Now, writing the compressed form of Eqns. (33)-(36) yields:

$$\ddot{\mathrm{A}}_1F_{s+1} = \ddot{\mathrm{E}}_1, \tag{39}$$

$$\ddot{\mathrm{A}}_2G_{s+1} = \ddot{\mathrm{E}}_2, \tag{40}$$

$$\ddot{\mathrm{A}}_3\theta_{s+1} = \ddot{\mathrm{E}}_3, \tag{41}$$

$$\ddot{\mathrm{A}}_4\phi_{s+1} = \ddot{\mathrm{E}}_4, \tag{42}$$

Where

$$\ddot{\mathrm{A}}_1 = \boldsymbol{D}, \ddot{\mathrm{E}}_1 = G_s, \tag{43}$$

$$\ddot{\mathrm{A}}_2 = (n-1)\boldsymbol{D}^2 + diag\left[a_{0,s}\right]\boldsymbol{D} - \frac{2}{m+1}diag\left[a_{1,s}\right]\boldsymbol{I}, \ddot{\mathrm{E}}_2 = B_{1,s}, \tag{44}$$

$$\ddot{\mathrm{A}}_3 = \boldsymbol{D}^2 + +P_r\left\{diag\left[b_{0,s}\right]\boldsymbol{D} + \frac{m-1}{m+1}diag\left[b_{1,s}\right]\boldsymbol{D} + N_t\boldsymbol{D}^2\right\}, \ddot{\mathrm{E}}_3 = B_{2,s}, \tag{45}$$

$$\ddot{\mathrm{A}}_4 = \boldsymbol{D}^2 + +L_e\left\{diag\left[c_{0,s}\right]\boldsymbol{D} + \frac{N_t}{N_b}diag[\theta''_{s+1}] - \frac{2}{m+1}\gamma - \frac{2}{m+1}diag\left[c_{1,s}\right]\right\}, \ddot{\mathrm{E}}_4 = B_{3,s}, \tag{46}$$

Where:

$$a_{0,s} = F_s\,, a_{1,s} = \,[Ha + \beta_D], B_{1,s} = G_s^2$$

$$+\left(\frac{2}{m+1}\right)F_r G_s^2 - \sqrt{\frac{(m+1)}{2}}\,nWeG'^2{}_sG''_s - Gr_b\theta_s - R_b\phi_s,$$

$$b_{0,s} = F_{s+1}\,,\;\; b_{1,s} = \eta G_{s+1} + N_b\phi'_s\,, B_{2,s} = 0,$$

$$c_{0,s} = F_{s+1} + \tfrac{m-1}{m+1}\eta G_{s+1}\,, c_{1,s} = (1+\delta\theta)^{m_1}e^{\left(\frac{-E}{1+\delta\theta}\right)}, B_{3,s} = 0, \qquad (47)$$

and

$$diag[a_{0,s}] = \begin{bmatrix} a_{0,s}(\eta_0) & \cdots & \\ \vdots & \ddots & \vdots \\ & \cdots & a_{0,s}(\eta_N) \end{bmatrix}, diag[a_{1,s}] = \begin{bmatrix} a_{1,s}(\eta_0) & \cdots & \\ \vdots & \ddots & \vdots \\ & \cdots & a_{1,s}(\eta_N) \end{bmatrix},$$

$$diag[b_{0,s}] = \begin{bmatrix} b_{0,s}(\eta_0) & \cdots & \\ \vdots & \ddots & \vdots \\ & \cdots & b_{0,s}(\eta_N) \end{bmatrix}, diag[b_{1,s}] = \begin{bmatrix} b_{1,s}(\eta_0) & \cdots & \\ \vdots & \ddots & \vdots \\ & \cdots & b_{1,s}(\eta_N) \end{bmatrix},$$

$$diag[B_{1,s}] = \begin{bmatrix} B_{1,s}(\eta_0) \\ \vdots \\ B_{1,s}(\eta_N) \end{bmatrix}, diag[c_{0,s}] = \begin{bmatrix} c_{0,s}(\eta_0) & \cdots & \\ \vdots & \ddots & \vdots \\ & \cdots & c_{0,s}(\eta_N) \end{bmatrix},$$

$$B_{1,s} = B_{2,s}B_{3,s} = \mathbf{0} = \begin{bmatrix} 0 \\ \vdots \\ 0 \end{bmatrix}. \qquad (48)$$

$F_{s+1} = [F(\eta_0), F(\eta_1), \ldots\,, F(\eta_N)\;]^T, G_{s+1} = [G(\eta_0), G(\eta_1), \ldots\,, G(\eta_N)\;]^T, \theta_{s+1} = [\theta(\eta_0), \theta(\eta_1), \ldots\,, \theta(\eta_N)\;]^T, \phi_{s+1} = [\phi(\eta_0), \phi(\eta_1), \ldots\,, \phi(\eta_N)\;]^T,$ are vectors of dimensions $(N+1)\times 1$. $\mathbf{0}$ is a vector of dimension $(N+1)\times 1$ and $\boldsymbol{I}$ describes the identity matrices of dimension $(N+1)\times(N+1)$.

The enforcement of boundary conditions on the system of Eqns. (43)-(46) are:

$$\ddot{\mathrm{A}}_1 = \begin{bmatrix} \ddot{\mathrm{A}}_1 \\ \hline 0 \quad \ldots \quad 1 \end{bmatrix}, F_{s+1} = \begin{bmatrix} F_{s+1}(\eta_0) \\ F_{s+1}(\eta_1) \\ \vdots \\ \hline F_{s+1}(\eta_N) \end{bmatrix}, \qquad \ddot{\mathrm{E}}_1 = \begin{bmatrix} \ddot{\mathrm{E}}_1 \\ \hline \frac{(1-m)\alpha_1}{m+1} \end{bmatrix},$$

$$\ddot{A}_2 = \begin{bmatrix} 1 & \dots & 0 \\ \hline & \ddot{A}_2 & \\ \hline 0 & \dots & 1 \end{bmatrix}, G_{s+1} = \begin{bmatrix} G_{s+1}(\eta_0) \\ \hline G_{s+1}(\eta_1) \\ \vdots \\ \hline G_{s+1}(\eta_N) \end{bmatrix}, \qquad \ddot{E}_2 = \begin{bmatrix} 0 \\ \hline \ddot{E}_2 \\ \\ \hline 1 \end{bmatrix},$$

$$\ddot{A}_3 = \begin{bmatrix} 1 & \dots & 0 \\ \hline & \ddot{A}_3 & \\ \hline 0 & \dots & 1 \end{bmatrix}, \theta_{s+1} = \begin{bmatrix} \theta_{s+1}(\eta_0) \\ \hline \theta_{s+1}(\eta_1) \\ \vdots \\ \hline \theta_{s+1}(\eta_N) \end{bmatrix}, \ddot{E}_3 = \begin{bmatrix} 0 \\ \hline \ddot{E}_3 \\ \\ \hline 1 \end{bmatrix}, \ddot{A}_4 = \begin{bmatrix} 1 & \dots & 0 \\ \hline & \ddot{A}_4 & \\ \hline 0 & \dots & 1 \end{bmatrix},$$

$$\phi_{t+1} = \begin{bmatrix} \phi_{s+1}(\eta_0) \\ \hline \phi_{s+1}(\eta_1) \\ \vdots \\ \hline \phi_{s+1}(\eta_N) \end{bmatrix}, \ddot{E}_4 = \begin{bmatrix} 0 \\ \hline \ddot{E}_4 \\ \\ \hline 1 \end{bmatrix}, \begin{bmatrix} 1 & \dots & 0 \\ \hline & B_5 & \\ \hline 0 & \dots & 1 \end{bmatrix}. \tag{49}$$

The pertinent earliest guesses are chosen as below:

$$F_0(\eta) = \frac{(1-m)\alpha_1}{m+1} + (1 - e^{-\eta}), G_0(\eta) = e^{-\eta}, \theta_0(\eta) = \phi_0(\eta) = \Phi_0(\eta) = e^{-\eta}. \tag{50}$$

The above earliest assumed approximated values obey the boundary conditions (37)-(38) and allow subsequent updating of the approximated values of $F_s, G_s, \theta_s, \phi_s$ to each $s = 1, 2, \dots \dots$by employing the SRM technique.

4.CONVERGENCE, ERROR AND STABILITY OF THE SRM ITERATION SCHEME

The convergence and stability of the current iterative SRM can be determined by considering the norms of the variation in the function values for two successive iterations. Therefore, towards every iteration, the maximal error (E_r) over the $(r + 1)^{\text{th}}$ iteration is prescribed as:

$$E_r = Max\left(\left\|f_{1,r+1} - f_{1,r}\right\|_\infty, \left\|f_{2,r+1} - f_{2,r}\right\|_\infty, \dots, \left\|f_{m,r+1} - f_{m,r}\right\|_\infty\right). \tag{51}$$

Whenever the numerical values from the iterations converge, the error E_r is predicted to drop with an increment in further iterations. The unknowns are approximated across the numbers of collocation points N, until the following test for convergence is satisfied on iteration r:

$$E_r \leq \varepsilon. \tag{52}$$

where ε is the convergence tolerance level and for the present study is prescribed as $\varepsilon = 10^{-7}$. The impact of the numbers of collocation points N are analyzed to choose the minimal values of

N that provide congruent solutions to the ε error level. This is accomplished through re-solving the governing equations utilizing the suggested iteration scheme with various values of N until consistent solutions are obtained.

5.VALIDATION OF SRM APPROACH WITH PREVIOUS STUDIES

Table 1 shows the comparison of SRM solutions with results from the literature to validate the SRM scheme. It is evident that excellent agreement is obtained with the shooting method solutions of Khan *et al.* [57] for the data prescribed in **Table 1** (bioconvection effects in [57] are negated for the comparison). SRM is therefore confirmed to be a reliable and adaptive method and confidence in the SRM solutions is justifiably very high.

Table 1. SRM solutions for $-\theta'(0)$ and $-\phi'(0)$ compared with Khan *et al.* [57] for various N_t and N_b values with $m = \alpha_1 = Ha = We = 0.1, Gr_b = R_b = \gamma = 0.5, P_r = L_e = 1.0, n = 1.2, \beta_D = F_r = \sigma_1 = \delta = E = 0.$

N_b	N_t	SRM results for $-\boldsymbol{\theta}'(\mathbf{0})$	Khan *et al.* [57] (shooting method) for $-\boldsymbol{\theta}'(\mathbf{0})$	SRM results for $-\boldsymbol{\phi}'(\mathbf{0})$	Khan *et al.* [57] (shooting method) for $-\phi'(0)$
0.1	0.1	1.345406	1.3453	1.435312	1.4353
0.2	0.1	1.103514	1.1035	1.113524	1.1135
0.3	0.1	1.005178	1.0051	1.006446	1.0064
0.1	0.1	1.345366	1.3453	1.435312	1.4353
0.1	0.2	1.215108	1.2151	1.315611	1.3156
0.1	0.3	1.112093	1.1120	1.112877	1.1128

6. RESULTS AND DISCUSSION

The SRM technique, together with the pseudo-spectral method, has been employed to compute the transport characteristics for reactive magnetohydrodynamic hyperbolic tangent nanofluid flow from a parabolic subsurface in non-Darcy porous media. The impact of the

emerging parameters on velocity, temperature and nano-particle concentration distributions is visualized in **Figs. 2-15**.

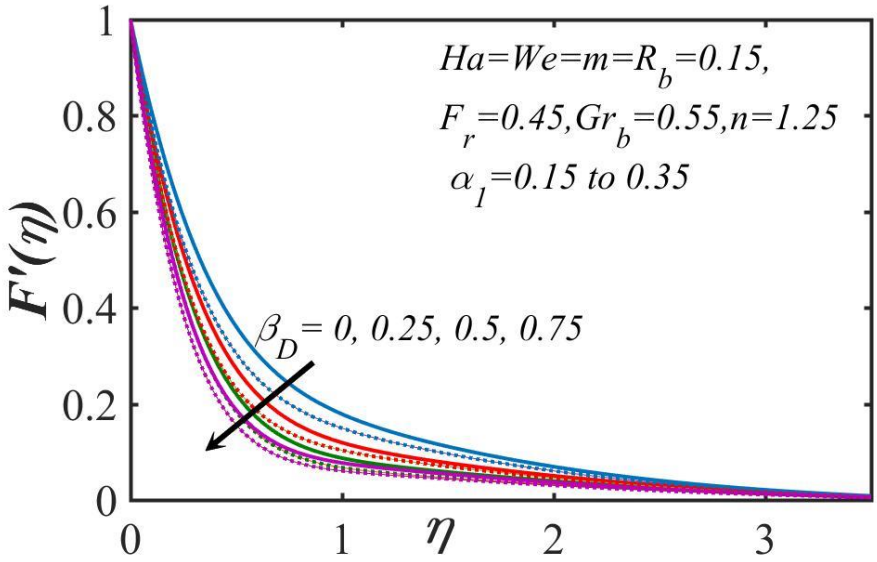

Fig. 2 Influence of β_D and α_1 on velocity profiles. Solid curve: $\alpha_1 = 0.15$, Dotted curve: $\alpha_1 = 0.35$.

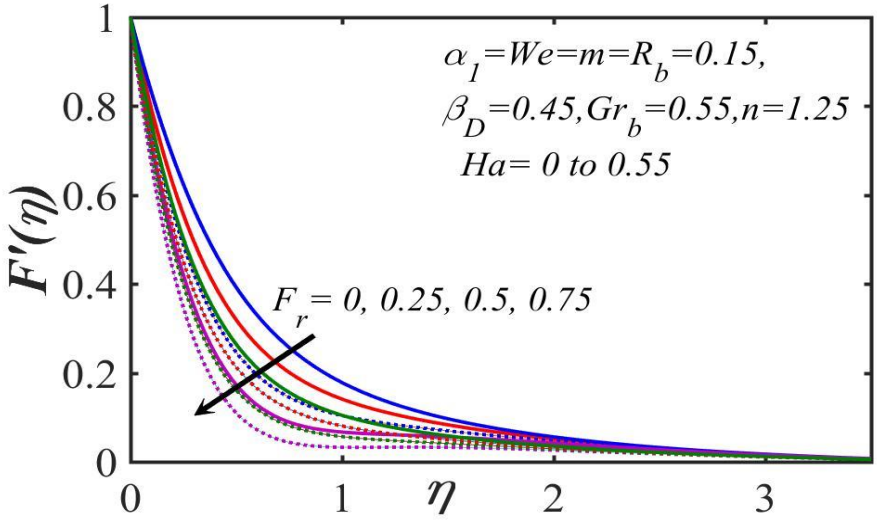

Fig. 3 Influence of F_r and Ha on velocity profiles. Solid curve: $Ha = 0$, Dotted curve: $Ha = 0.55$.

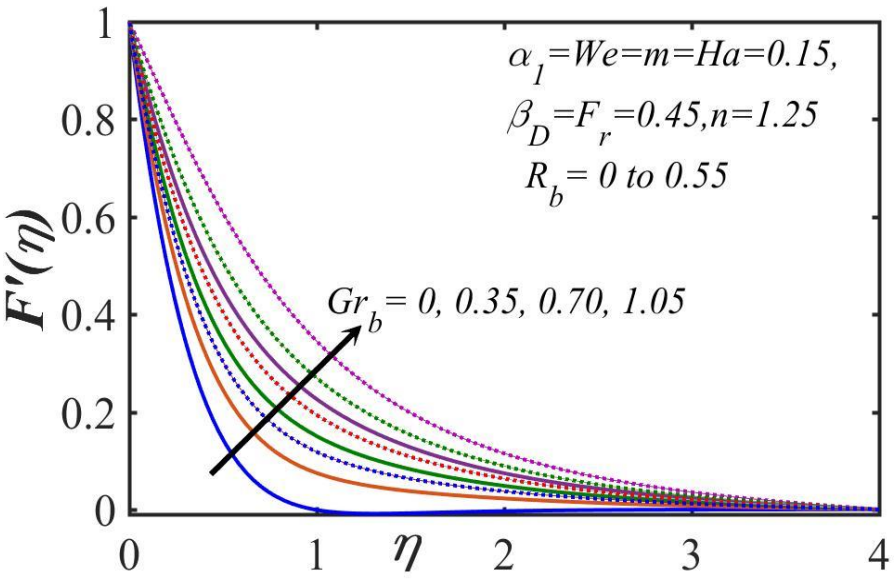

Fig. 4 Impact of Gr_b and R_b on velocity distributions. Solid curve: $R_b = 0$, Dotted curve: $R_b = 0.55$.

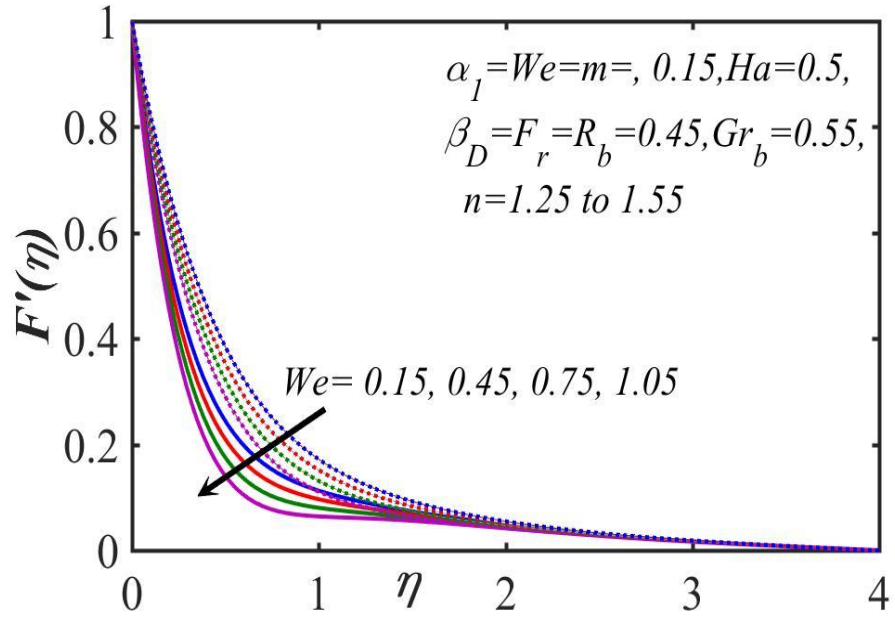

Fig. 5 Effects of We and m on velocity distribution. Solid curve: $n = 1.25$, Dotted curve: $n = 1.55$.

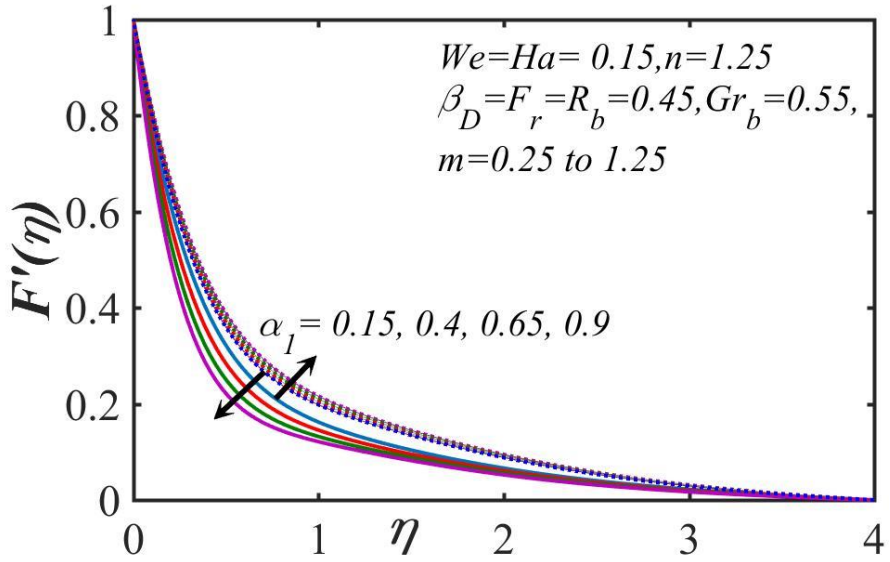

Fig. 6 Influence of α_1 and m on velocity profiles. Solid curve: $m = 0.25$, Dotted curve: $m = 1.25$.

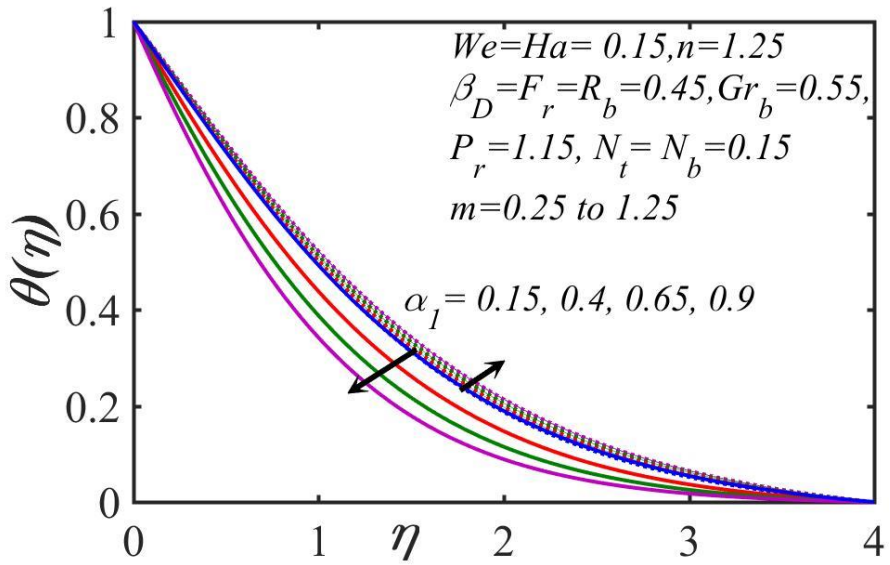

Fig. 7 Impact of α_1 and m on temperature profiles. Solid curve: $m = 0.25$, Dotted curve: $m = 1.25$.

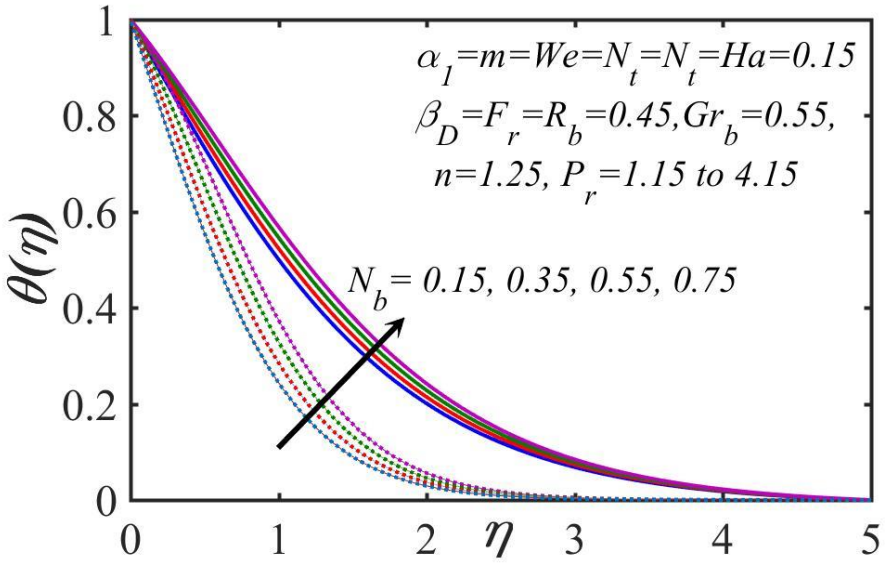

Fig. 8 Impact of N_b and P_r on temperature magnitudes. Solid curve: $P_r = 1.15$, Dotted curve: $P_r = 4.15$.

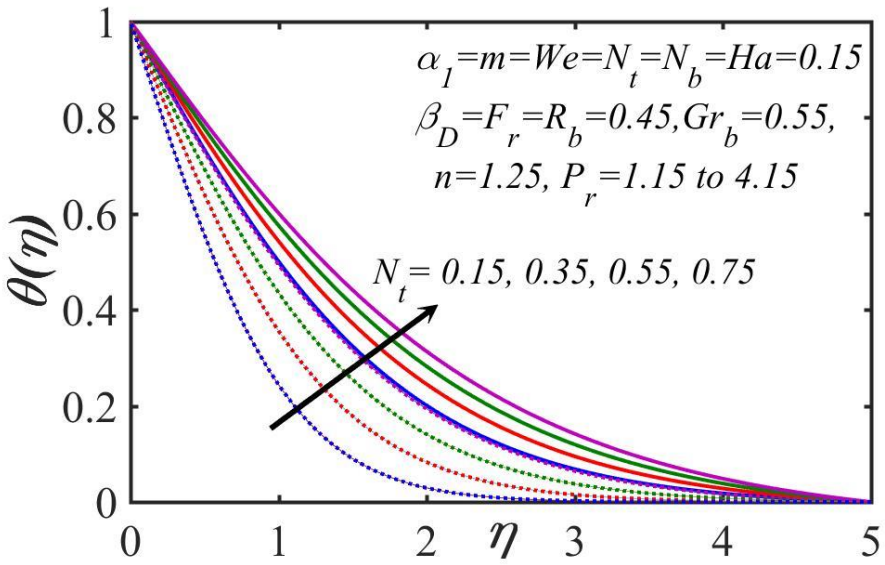

Fig. 9 Variation of N_t and "P_r" on temperature magnitudes. Solid curve: $P_r = 1.15$, Dotted curve: $P_r = 4.15$.

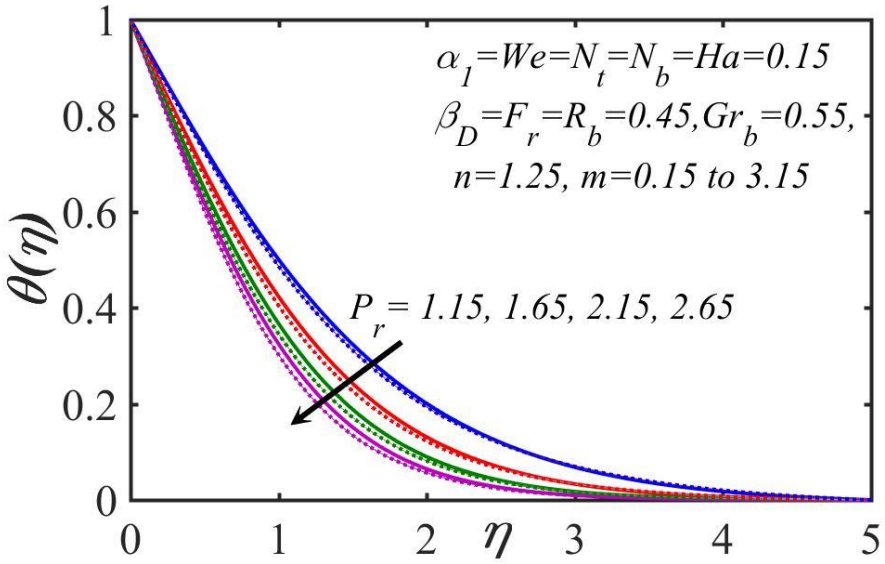

Fig. 10 Impact of P_r and "m" on temperature profiles. Solid curve: $m = 0.15$, Dotted curve: $m = 3.15$.

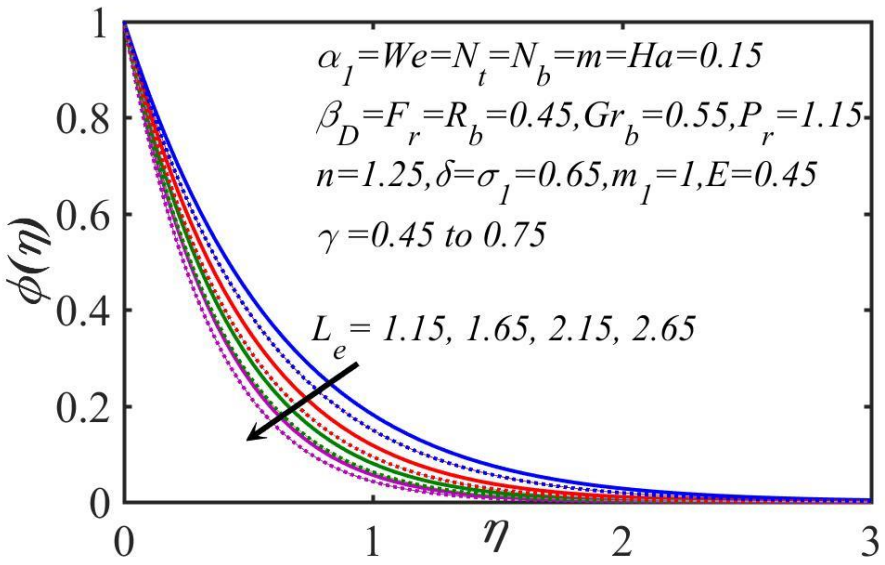

Fig. 11 Influence of L_e and "γ" on concentration magnitudes. Solid curve: $\gamma = 0.45$, Dotted curve: $\gamma = 0.75$.

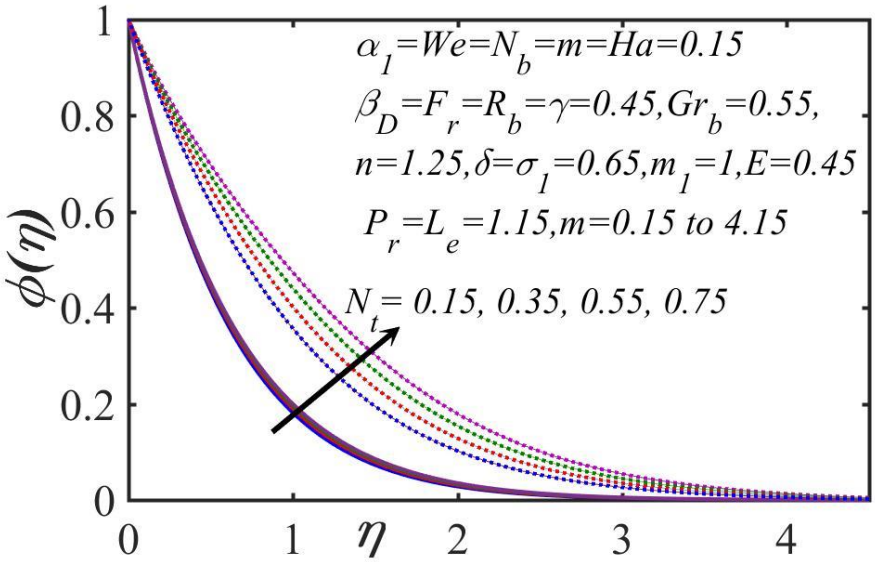

Fig. 12 Influence of N_t and m on the concentration magnitudes. Solid curve: $m = 0.15$, Dotted curve: $m = 4.15$.

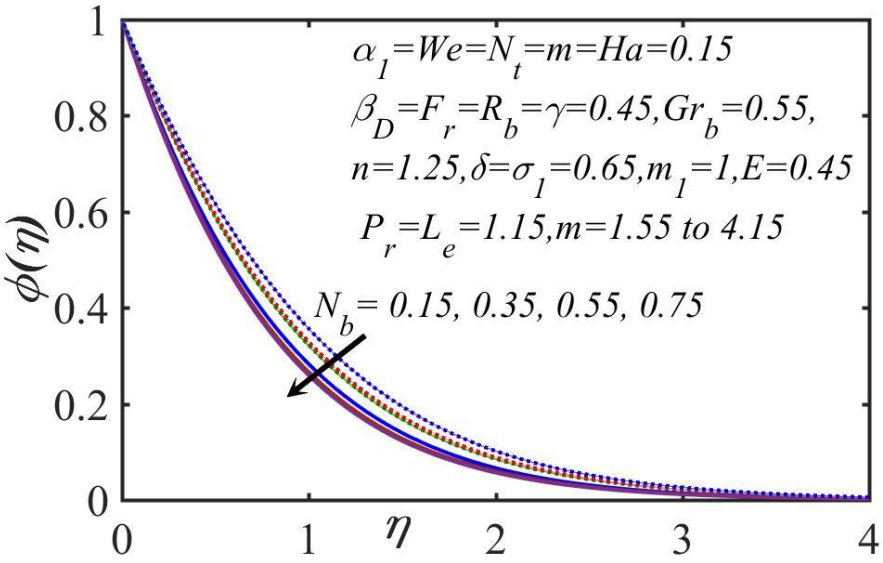

Fig. 13 Variation of N_b and m on the concentration magnitudes. Solid curve: $m = 1.55$, Dotted curve: $m = 4.15$.

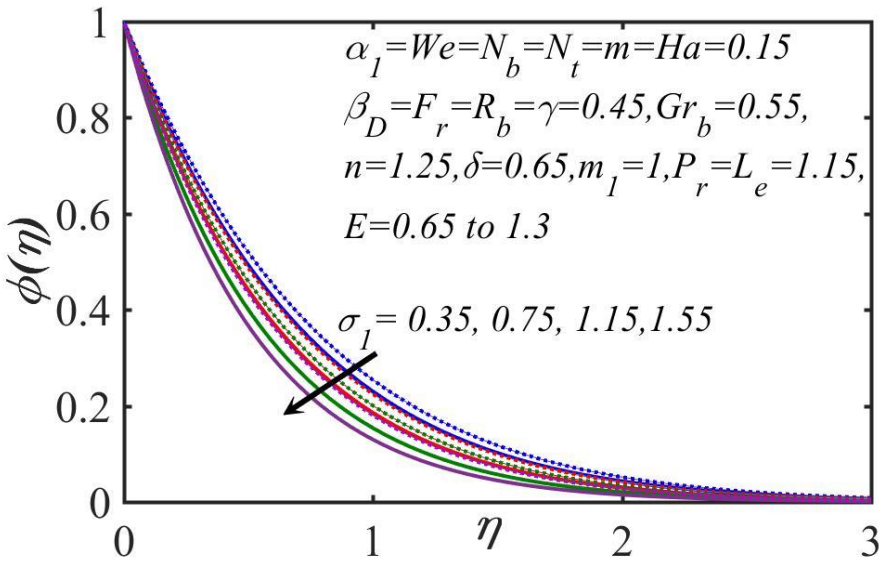

Fig. 14 Influence of σ_1 and E on the concentration magnitudes. Solid curve: $E = 0.65$, Dotted curve: $E = 1.3$.

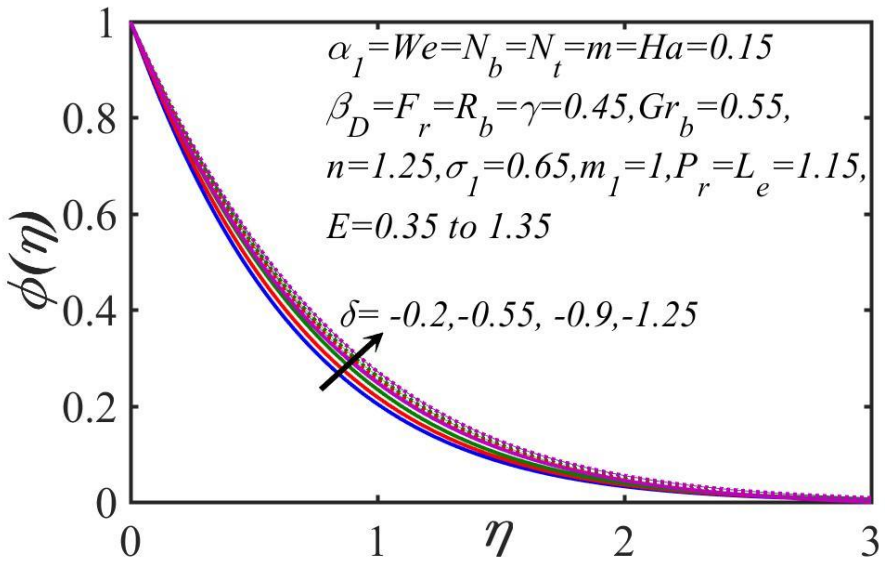

Fig. 15 Impact of δ and E on the concentration magnitudes. Solid curve: $E = 0.35$, Dotted curve: $E = 1.35$.

Table 2. SRM solutions for skin-friction coefficient for various $N, Ha,$ and We with $m = \alpha_1 = 0.1, Gr_b = R_b = 0.5, , n = 1.2, \beta_D = F_r = 0.$

N	Ha	We	$\frac{C_{Fx}}{Re_x^{1/2}}$
45	0.1	0.1	0.5528
55	0.1	0.1	0.5539
65	0.1	0.1	0.5549
90	0.1	0.1	0.5549
45	0.2	0.1	0.4841
55	0.2	0.1	0.4852
65	0.2	0.1	0.4861
90	0.2	0.1	0.4861
45	0.3	0.1	0.4022
55	0.2	0.1	0.4033
65	0.1	0.1	0.4041
90	0.1	0.1	0.4041
45	0.1	0.2	0.5535
55	0.1	0.2	0.5547
65	0.1	0.2	0.5556
90	0.1	0.2	0.5556
45	0.1	0.3	0.5543
55	0.1	0.3	0.5554
65	0.1	0.3	0.5562
90	0.1	0.3	0.5562

It is important to note that all data used is carefully selected to be representative of actual coating flows of magnetic nanofluids and is extracted from [66-69]. Other data is taken from Khan *et al.* [55] and Khan *et al*. [70]. In particular, *weak magnetic field* is studied i.e. *Ha* < 1 for which the Lorentzian magnetic body force is weak and therefore Hall current effects are not invoked [71]. **Fig. 2** illustrates the influence of β_D and α_1 on velocity magnitudes. It is seen that velocity is

reduced with increment in both permeability parameter β_D and wall thickness α_1. Momentum boundary layer thickness is therefore enhanced with both these parameters since the flow is decelerated. Permeable parameter β_D ($= \frac{\mu_f}{U_0(x+b)^{m-1}k}$) arises in the term, $-\frac{2}{m+1}(\beta_D F')$ in the dimensionless momentum Eqn. (8). This is the *Darcian term* and is a drag force associated with bulk porous medium fibers. This term is inversely proportional to the actual permeability of the porous medium, *k*. As β_D increases therefore the permeability is reduced. This produces greater solid fiber resistance to the nanofluid and results in flow deceleration. Although a retardation is also induced with greater wall thickness parameter, α_1, the effect is not as prominent as with increment in permeability parameter which may be attributable to the wall thickness parameter, arising only in the wall boundary condition (11) i.e. $F(0) = \frac{(1-m)\alpha_1}{m+1}$. Asymptotically smooth convergence of all profiles from the wall (parabola surface) to the free stream is also achieved confirming the selection of a suitably large infinity boundary condition in the SRM computations. **Fig. 3** shows the influence of Forchheimer (quadratic porous medium drag) parameter F_r and Hartmann number Ha on velocity distributions is shown. Significant retardation in the flow is induced with larger Hartmann number Ha and also greater Forchheimer parameter F_r. Both parameters are associated with drag forces i.e. the terms $-\frac{2}{m+1}(F_r F'^2)$ and $-\frac{2}{m+1}(HaF')$ in Eqn. (8). Whereas the Forchheimer drag term is quadratic, the Lorentzian magnetic drag term is linear. As *Ha* is increased the resistive Lorentz force (which is directed transverse to the magnetic field and therefore acts along the parabola surface) is also increased relative to the *inertial hydrodynamic force*, as per the definition of the modified Hartmann number ($Ha = \frac{\sigma {B_0}^2}{\rho U_0(x+b)^{m-1}}$). Velocity is therefore maximum for the electrically non-conducting case (*Ha* =0) for which a thinner momentum boundary layer is produced. With *Ha* = 0.55, the velocity is reduced, and the momentum boundary layer is thicker. Both magnetic parameter and Forchheimer parameter effectively achieve significant damping of the flow field.

Fig. 4 portrays the impact of thermal and concentration Grashof numbers i.e. Gr_b and R_b on velocity magnitudes. Increasing thermal Grashof number $Gr_b = \frac{\tilde{g}\beta(T_w - T_\infty)}{(x+b)^{2m-1}{U_0}^2}$ implies a greater thermal buoyancy force contribution and increasing concentration (solutal) Grashof number, $R_b = \frac{\tilde{g}(C_w - C_\infty)}{(x+b)^{2m-1}{U_0}^2}$ corresponds to a larger nanoparticle species buoyancy force contribution.

Velocity is enhanced with increment in both Grashof numbers i.e. the flow is accelerated and there is a concomitant decrease in momentum (hydrodynamic) boundary layer thickness. Significant escalation in the flow is therefore achieved with thermal and species buoyancy forces.

Fig. 5 shows that the movement of fluid decelerates for taking increment in Weissenberg number We and escalates for the power-law index n. $We = \sqrt{\frac{{U_0}^3 (x+b)^{3m-3}}{\nu}}\Gamma$ and is used to quantify viscoelastic behaviour and expresses the ratio of elastic force to viscous force in the boundary layer. It also defines the ratio of the relaxation time of the fluid and a specific process time. *We* appears only in the augmented shear diffusion term, $+\sqrt{\frac{(m+1)}{2}}nWeF''F'''$ in the momentum equation (8). As *We* is elevated, the elastic force is increased relative to the viscous force (and the relaxation time is reduced. This decelerates the boundary layer flow, as also observed in Gaffar *et al.* [40] and Hayat *et al.* [41] and enhances momentum boundary layer thickness. With increment in tangent hyperbolic nanofluid power-law index n, however, the opposite trend is produced and velocity is elevated. The nanofluid boundary layer thickness on the parabola surface is therefore reduced with increasing power-law index. The parameter *n* is also used to characterize the rheology of the tangent hyperbolic nanofluid. It features in the highest order shear term, $(n-1)F'''$ and also the term, $\sqrt{\frac{(m+1)}{2}}nWeF''F'''$. Overall, this parameter aids in momentum development on the substrate whereas Weissenberg number opposes momentum diffusion.

Fig. 6 displays the influence of wall thickness, α_1 and stretching index m. Whereas the parameter, α_1 appears only in the boundary condition (8), the parameter m features in multiple terms in not only the momentum eqn. (8) but also the energy eqn. (9) and nanoparticle concentration eqn. (10). It is noted that increasing values in α_1 causes a decrement in the velocity magnitudes and increases momentum boundary layer thickness for $m < 1$, whereas it enhances the velocity and decreases momentum boundary layer thickness with $m > 1$. The stretching velocity of the coating on the parabola substrate is increased with power-law stretching parameter, m. This aids in momentum diffusion and leads to flow acceleration in the boundary layer.

Figs. 7-10 depict the impact of Prandtl number P_r, thermophoresis parameter N_t, Brownian motion parameter N_b, wall thickness α_1, and stretching parameter, m on temperature magnitudes. It can be seen from **Fig. 7**, that an increment in α_1 produces a decrement in temperature and decreases thermal boundary layer thickness adjacent to the substrate for $m < 1$, whereas the

opposite trend (temperature enhancement and thicker thermal boundary layer) is computed for $m > 1$. Effectively greater wall thickness induces heating in the regime, for $m > 1$, and produces cooling for $m < 1$. **Figs. 8-9** show that with elevation in N_t and N_b, there is an escalation in both temperature magnitudes and thermal boundary layer thicknesses. Greater thermophoretic body force in the nanofluid encourages the migration of nanoparticles under a thermal gradient and boosts thermal diffusion. Similarly, with greater Brownian motion parameter, the nanoparticles are reduced in size (as per the Buongiorno model [10]) which exacerbates heat diffusion in the regime. In contrast, increasing Prandtl number P_r reduces temperatures since thermal conductivity is reduced (Prandtl number is inversely proportional to thermal conductivity for a fixed value of dynamic viscosity and specific heat capacity). Thermal boundary layer thickness is also therefore decreased. Prandtl number also expresses the ratio of momentum diffusion rate to thermal diffusion rate. For higher Prandtl number, lower thermal diffusion rates arise, and this explains the decrement in temperature for $P_r = 4.15$ compared with $P_r = 1.15$. **Fig. 10** confirms these trends showing again that temperature is suppressed with increasing stretching parameter index, m and increasing Prandtl number, P_r.

Figs. 11-15 visualize the influence of Lewis number L_e, stretching parameter index m, thermophoresis parameter N_t, Brownian-motion parameter N_b, chemical reaction rate parameter, γ, chemical reaction constant σ_1, temperature ratio parameter δ, and activation energy parameter E, on nano-particle concentration distributions. From **Fig. 11**, it is evident that greater L_e strongly *reduces* the nanoparticle concentration magnitudes. Lewis number characterizes the ratio of thermal diffusion to nanoparticle diffusion and also expresses the relative thickness of the thermal boundary layer to the nanoparticle species boundary layer. Since all values of L_e considered are in excess of unity, the nanoparticle species diffusion rate is always lower than thermal diffusion rate. Nanoparticle concentrations are therefore suppressed with increasing L_e. Maximum nanoparticle concentration clearly corresponds to the minimum magnitude of L_e. It is also observed that with higher values of chemical reaction rate parameter, γ the nano-particle concentration decreases. This parameter arises in the term, $-\frac{2}{m+1}\gamma\phi$ in the nanoparticle concentration eqn. (10). Higher values of the reaction rate imply greater conversion of the original nanoparticles to a new species and therefore the original concentration is depleted. Nanoparticle species boundary layer thickness is also reduced with increase in chemical reaction rate parameter, γ from 0.45 (solid line) to 0.75 (dotted lines). From **Figs. 12-13**, it is apparent that there is an escalation in both concentration

magnitudes with larger values of stretching parameter index m. However, concentration magnitudes *increase* with higher values of N_t whereas they *decrease* with greater N_b. Fig. 14. Illustrates the impact of chemical reaction constant σ_1 and the activation energy E parameter on nano-particle concentration, ϕ. There is a reduction in nanoparticle concentration with greater values of σ_1, whereas it is increased with an increment in activation energy parameter, E. Therefore, nanoparticle species boundary layer thickness is therefore suppressed with higher values of chemical reaction constant σ_1 whereas it is boosted with higher activation energy parameter, E. Finally, **Fig. 15** indicates that nanoparticle concentration is enhanced with increasingly negative values of the temperature ratio, δ and species boundary layer thickness is therefore also reduced. Once again however with an increase in activation energy parameter, E.

Table 2 displays the numerical results of $C_{Fx}/Re_x^{1/2}$ for number of collocation points in the SRM code, N, Weissenberg number, We, and modified Hartmann magnetic number, Ha keeping all other parameters fixed. Very good stability of results is obtained for different collocation point number. With increasing Weissenberg number, *We*, there is a considerable increase in skin friction magnitudes. With greater magnetic parameter, *Ha*, there is also a significant decrease in skin friction indicating greater retardation of the flow in the boundary layer adjacent to the parabolic substrate with stronger applied magnetic field.

7. CONCLUDING REMARKS

Motivated by emerging applications in magnetic smart Nano coating systems, in this article, a theoretical study of *magnetohydrodynamic tangent hyperbolic non-Newtonian nanofluid flowing from a stretching upper parabolic substrate geometry with chemical reaction and activation energy in non-Darcy porous media, has been presented*. The *Darcy-Brinkman-Forchheimer model for porous media effects has been utilized*. The governing partial differential equations are rendered into ordinary differential equations via appropriate similarity transformations. The resulting nonlinear boundary value problem is solved numerically by employing the spectral relaxation method (SRM) and validation is included with earlier studies. Numerical results for velocity, temperature and nanoparticle concentration are visualized graphically for the influence of key emerging parameters. Tables for skin friction, Nusselt number and Sherwood number are also presented. The principal observations of the current study may be summarized as follows:

i. Velocity is decreased with an elevation in wall thickness parameter, permeability parameter, Forchheimer (quadratic porous media drag) parameter, Weissenberg number and modified Hartmann magnetic number. There is a corresponding increase in the momentum boundary layer thickness over the stretched parabolic subsurface.

ii. Velocity is enhanced with increment in stretching index, tangent hyperbolic rheological power-law index, thermal Grashof number and species (solutal) Grashof number, and an associated reduction in the momentum boundary layer thickness.

iii. The velocity and temperature magnitudes adjacent to the subsurface are reduced with an increment in wall thickness parameter for stretching index < 1, whereas the opposite behaviour is computed for stretching index > 1.

iv. Temperature magnitudes are depleted (i.e. cooling is induced) with increment in stretching index and Prandtl number; however, the temperatures are boosted with increasing Brownian motion and thermophoresis parameters.

v. Nano-particle concentration magnitudes are reduced with greater Lewis number and Brownian motion parameter; however, magnitudes are elevated with increasing values of the stretching index and thermophoresis parameter.

vi. Nano-particle concentration magnitude is suppressed with increasing values of the chemical reaction constant whereas they are elevated with increment in activation energy parameter.

vii. Skin friction is strongly suppressed with greater modified Hartmann number whereas it is enhanced with increment in Weissenberg number.

viii. The spectral relaxation method (SRM) demonstrates excellent accuracy and numerical stability for solving nonlinear boundary value problems of multi-physical reactive magnetic rheological nanofluid coating materials processing on complex surfaces. Future studies may consider alternative non-Newtonian models e.g. Eringen's micropolar model [59] and will be communicated imminently.

REFERENCES

[1] S.U. Choi, *J. Heat Transf.* **231**, 99 (1995).

[2] M.A. Khairul *et al.*, *Int. J. Heat Mass Transf.* **98**, 778 (2016).

[3] S.K. Das *et al.*, *Nanofluids-Science and Technology*, Wiley, New York, (2008).

[4] S. Kuharat *et al.*, *Arab. J. Sci. Eng.* **45**, 9075 (2020).

[5] Y. Zhang *et al., J. Mater. Process. Technol.* **232**, 100-115 (2016).

[6] L. Zhang *et al., J. Nanopart. Res.* **9**, 479 (2007).

[7] K. Hadad and Z. Kowsar, *Ann. Nucl. Energy* **97**, 179-182 (2016).

[8] R. N. Mehta *et al.*, *Fuel* **120**, 91 (2014).

[9] B. Thiesen and A. Jordan, *Int. J. Hyperthermia* **24**, 467 (2008).

[10] J. Buongiorno, *J. Heat Transf.* **128**, 240 (2006).

[11] R. Tiwari, S. Das, *Int. J. Heat Mass Transf.* **50**, 2002 (2007).

[12] S. Kakaç, A. Pramuanjaroenkij, *Int. J. Heat Mass Transf.* **52**, 3187 (2009).

[13] A. A. Tracton (Ed)., *Coatings Technology Handbook*, CRC Press, 3rd edn, USA (2005).

[14] S. Abdul Gaffar *et al., Comput. Therm. Sci.* **12**, 329 (2020).

[15] Mohamed Gad-el-Hak, *Prog. Aerosp. Sci.* **38**, 77 (2002).

[16] J. Tao *et al., Chinese J. Aeronaut.* **32**, 577 (2019).

[17] N. Bachok *et al., Int. J. Therm. Sci*. **49**, 1663 (2010).

[18] H. Thameem Basha *et al.*, *J. Therm. Anal. Calorim.* **143,** 2273 (2021).

[19] Z. Haddad *et al., Int. J. Therm. Sci*. **57**, 152-162 (2012).

[20] M. Mustafa *et al., PLoS One* **8**, e61859 (2013).

[21] J. A. Khan *et al., PLoS One* **10**, e0116603 (2015).

[22] A. K. Ray *et al., Inventions* **4**, 1 (2019).

[23] S. Zhang and D. Zhao, *Advances in Magnetic Materials Processing, Properties, and Performance*, CRC Press, Florida, USA (2017).

[24] S. Tochihara, *Prog. Org. Coat.* **10,** 195 (1982).

[25] D.A. Weidner, *Phys. Fluids* **29**, 052103 (2017).

[26] D. T. Conroy and O. K. Matar, *Phys. Fluids*, **27**, 092102 (2015).

[27] A. Triwikantoro *et al., J. Supercond. Nov. Magn.* **30**, 555–560 (2017).

[28] Q. Liu *et al., Chem. Mater.* **10**, 12, 3936–3940 (1998).

[29] V. K. Thakur and M.R. Kessler, *Polymer Nanocomposites: New Advanced Dielectric Materials for Energy Storage Applications*, Springer, USA (2014).

[30] W. Ibrahim, B. Shankar, *Comput. Fluids* **75**, 1 (2013).

[31] W. Ibrahim *et al., Int. J. Heat Mass Transf.* **56**, 1 (2013).

[32] F. Mabood *et al., J. Magn. Magn. Mater.* **374**, 569 (2015).

[34] H. M. R. Gonçalves *et al.*, *Small*, **16,** 2070156 (2020).

[35] A. Hiremath *et al.*, *Arab. J. Sci. Eng.* **44,** 7875 (2019).

[36] T. Javed *et al.*, *Chem. Eng. Commun.* **200**, 327-336 (2013).

[37] O. A. Bég *et al.*, *J. Nanofluids* **7**, 1 (2018).

[38] Q. Nguyen, *et al.*, Math. Methods Appl. Sci. (2020). https://doi.org/10.1002/mma.6513

[39] S.U. Khan *et al.*, *J. Non-Equil. Thermodyn*. **45**, 81 (2020).

[40] S. Abdul Gaffar *et al.*, *J. Braz. Society Mech. Sci. Eng.*, 39:101–116 (2017).

[41] M. Nazeer *et al.*, *Int. J. Mod. Phys. B* 2150204 (2021).

[42] M. Nazeer *et al.*, *Int. J. Mod. Phys. B* 2150188 (2021).

[43] M. Nazeer *et al.*, *Int. Commun. Heat Mass Transf.* **119**, 104968 (2021).

[44] L. Zhang *et al.*, *Entropy* **22**, 1070 (2021).

[45] J. C. Umavathi and O. Anwar Bég, *Microfluid. Nanofluid.* **25,** 53 (2021).

[45] MD. Shamshuddin *et al.*, *Heat Transf.* (2020). DOI: 10.1002/htj.21963

[47] M. M. Bhatti *et al.*, *Arch. Appl. Mech.* **91,** 1683 (2021).

[48] N.S. Elgazery, *J. Egypt. Math. Soc.* **27,** 39 (2019).

[49] M. Jawad *et al., J. Phys. Commun.* **2** 115014 (2018).

[50] A.R. Bestman, *Int. J. Energy Res*. **14**, 389 (1990).

[51] O.D. Makinde *et al.*, *Afr. Mat.* **22**, 65–78 (2011).

[52] A. Hamid *et al.*, *J. Mol. Liq*. **262**, 435 (2018).

[53] M. Irfan *et al.*, *J. Phys. Chem. Solids*. **125**, 141 (2019).

[54] A. Zeeshan *et al.*, *Results Phys*. **8**, 502 (2018).

[55] S.U. Khan *et al.*, *Phys. Scr*. **94**, 125211 (2019).

[56] M. M. Bhatti *et al.*, *Processes* **8**, 328 (2020)

[57] M. Khan *et al.*, *Physica A* **553**, 124231 (2020).

[58] S. S. Motsa, *Chem. Eng. Commun.* **201**, 241 (2012).

[59] O. Anwar Bég *et al.*, *J. Engin. Thermophys.* **25,** 576–599 (2016).

[60] M. Marin, *J. Vib. Control* **16**, 33 (2010).

[61] I. A. Abbas and M. Marin, *Iran. J. Sci. Technol. Trans. Mech. Eng.* **42**, 57 (2018).

[62] M. Nazeer, *SN Appl. Sci.* **3**, 1 (2021).

[63] M. Turkyilmazoglu, *J. Aerosp. Eng.* **29**, 04016049 (2016).

[64] M. Turkyilmazoglu, *Eur. Phys. J. Plus* **136**, 1 (2021).

[65] M. Turkyilmazoglu, *Arch. Mech.* **71**, 49 (2019).

[66] Y. Zhang, *Nanofluids Research, Development and Applications*, Nova Science, USA (2013).

[67] D. Tripathi and R.K. Sharma (eds), *Energy Systems and Nanotechnology, Advances in Sustainability Science and Technology Book Series, Springer-Nature, India* (2021).

[68] Y. Liu, David J. Sellmyer and Daisuke Shindo, *Handbook of Advanced Magnetic Materials, Volume I: Advanced Magnetic Materials: Nanostructural Effects*, Springer China (2006).

[69] M. Turkyilmazoglu, *Numer. Heat Transf.; A: Appl.* **57**, 40 (2010).

[70] J. A. Khan *et al.*, (2017). *Int. J. Numer. Method H.* **27,** 221 (2017).

[71] S. Asai, *Electromagnetic Processing of Materials: Materials Processing by Using Electric and Magnetic Functions*, Springer, Netherlands (2012).